Geophysical Prospecting

EAGE EUROPEAN ASSOCIATION OF GEOSCIENTISTS & ENGINEERS

Geophysical Prospecting, 2014, **62**, 223–243 doi: 10.1111/1365-2478.12080

Retrieval of local surface wave velocities from traffic noise – an example from the La Barge basin (Wyoming)

M. Behm[1]*, Garrett M. Leahy[2] and R. Snieder[1]

[1]*Department of Geophysics, Colorado School of Mines, Golden, CO, USA,* [2]*Dept of Geology and Geophysics, Yale University, New Haven, CT, USA*

Received September 2012, revision accepted April 2013

ABSTRACT

In regions where active source seismic exploration is constrained by limitations of energy penetration and recovery, cost and logistical concerns, or regulatory restrictions, analysis of natural source seismic data may provide an alternative. In this study, we investigate the feasibility of using locally-generated seismic noise in the 2–6 Hz band to obtain a subsurface model via interferometric analysis. We apply this technique to three-component data recorded during the La Barge Passive Seismic Experiment, a local deployment in south-western Wyoming that recorded continuous seismic data between November 2008 and June 2009. We find traffic noise from a nearby state road to be the dominant source of surface waves recorded on the array and observe surface wave arrivals associated with this source up to distances of 5 kms. The orientation of the road with respect to the deployment ensures a large number of stationary points, leading to clear observations on both in-line and cross-line virtual source-receiver pairs. This results in a large number of usable interferograms, which in turn enables the application of standard active source processing methods like signal processing, common offset stacking and traveltime inversion. We investigate the dependency of the interferograms on the amount of data, on a range of processing parameters and on the choice of the interferometry algorithm. The obtained interferograms exhibit a high signal-to-noise ratio on all three components. Rotation of the horizontal components to the radial/transverse direction facilitates the separation of Rayleigh and Love waves. Though the narrow frequency spectrum of the surface waves prevents the inversion for depth-dependent shear-wave velocities, we are able to map the arrival times of the surface waves to laterally varying group and phase velocities for both Rayleigh and Love waves. Our results correlate well with the known geological structure. We outline a scheme for obtaining localized surface wave velocities from local noise sources and show how the processing of passive data benefits from a combination with well-established exploration seismology methods. We highlight the differences with interferometry applied to crustal scale data and conclude with recommendations for similar deployments.

Key words: Surface wave, Interferometry, Seismology.

1 INTRODUCTION

Passive seismology is gaining increased interest in the subsurface imaging community. Applications range from monitoring subsurface fluid injection and fault mapping to imaging basin-scale tectonic features. For imaging problems, the methodologies used so far typically draw heavily from methods established in the field of crustal seismology (e.g., teleseimic inversion, interferometry, receiver functions) and there is a natural focus on medium- to large-scale structures. In

*E-mail: mbehm@mines.edu

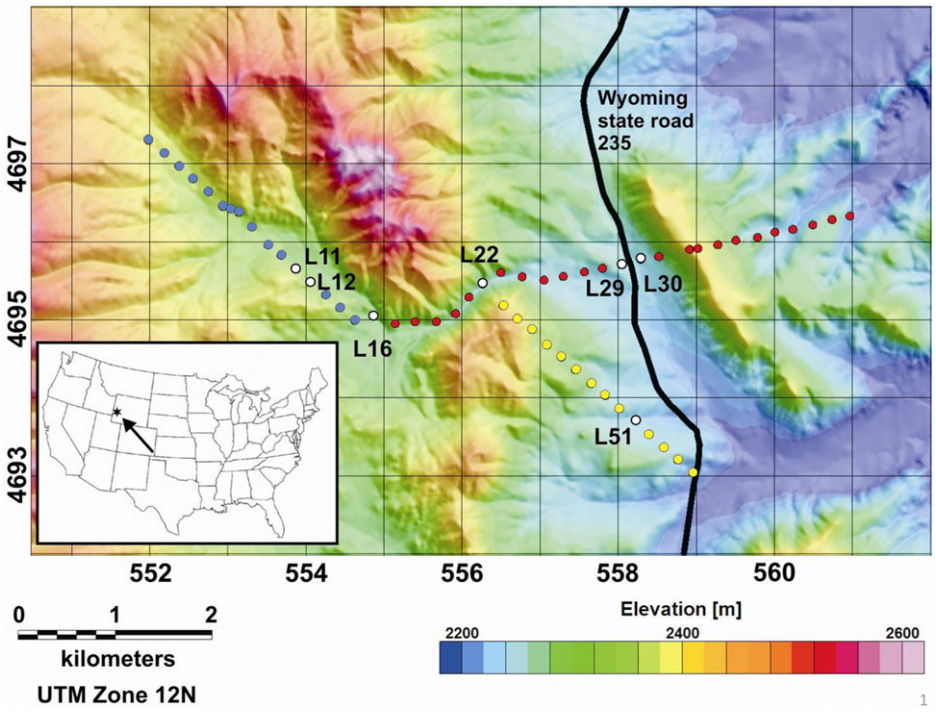

Figure 1 Location of deployment Blue circles: stations L01–L15 (segment 1); red circles: stations L19–L41 (segment 2); yellow circles: stations L42–L55 (segment 3). White circles denote virtual sources for which data and interferogram examples are shown in the following figures. Labels of map axes are UTM coordinates in kilometres.

terms of scale and geological variability, the different settings of local targets require modified processing schemes and may require choices of parameters that deviate strongly from the standards in global and regional studies.

In particular, there is much interest in 'ambient noise' or 'daylight imaging' techniques, in which a local structure is recovered via interferometric processing. These techniques are enticing in that no active sources are required and a deployment of only a few days may be sufficient to obtain a detailed subsurface image. Most commonly, frequency-dependant surface wave velocities are obtained and inverted for the vertical shear-wave velocity structure. While there is vast literature on the application of so-called ambient noise tomography on a continental scale (e.g., see the overview given by Bensen *et al.* 2007), the number of studies related to local targets is relatively limited. de Ridder and Dellinger (2011) obtained Scholte-wave velocity maps from ocean bottom measurements at the Valhall field offshore Norway on a spatial scale comparable to our study. Bussat and Kugler (2009) investigated an approximately 100 km^2 wide offshore area in the North Sea and derived depth-dependant shear-wave velocities from Rayleigh waves. In contrast, Picozzi *et al.* (2009) analysed a higher frequency range and subsequently obtained a three-dimensional shear-wave velocity image at a 100 by 100 m sized test site. Forghani and Snieder (2010) outlined why it is more difficult to retrieve body waves from interferometry, although several papers demonstrate the applicability on a local scale (e.g. O'Connell 2007; Draganov *et al.* 2009). Dong, He and Schuster (2006) and Halliday *et al.* (2007) used interferometry to predict and suppress ground roll from active source seismic data.

In general, these and similar studies suggest potential but there are few high-quality data sets available to test and benchmark these concepts against other imaging techniques. One such data set was collected over the La Barge Field in western Wyoming (Fig. 1). The **L**a Barge **P**assive **S**eismic **E**xperiment (LPSE; Saltzer *et al.* 2011) was a collaboration between ExxonMobil Upstream Research Co. and researchers at the University of Arizona. In this experiment, instruments from the National Science Foundation's PASSCAL facility were deployed for a period of approximately 8 months over a producing hydrocarbon basin. From November 2008–May 2009, 55 three-component broadband seismometers (Guralp CMG-3T) were continuously recording at a sample rate of 100 Hz. The station spacing in this experiment (250 m) was much narrower than the typical configuration for such sensitive

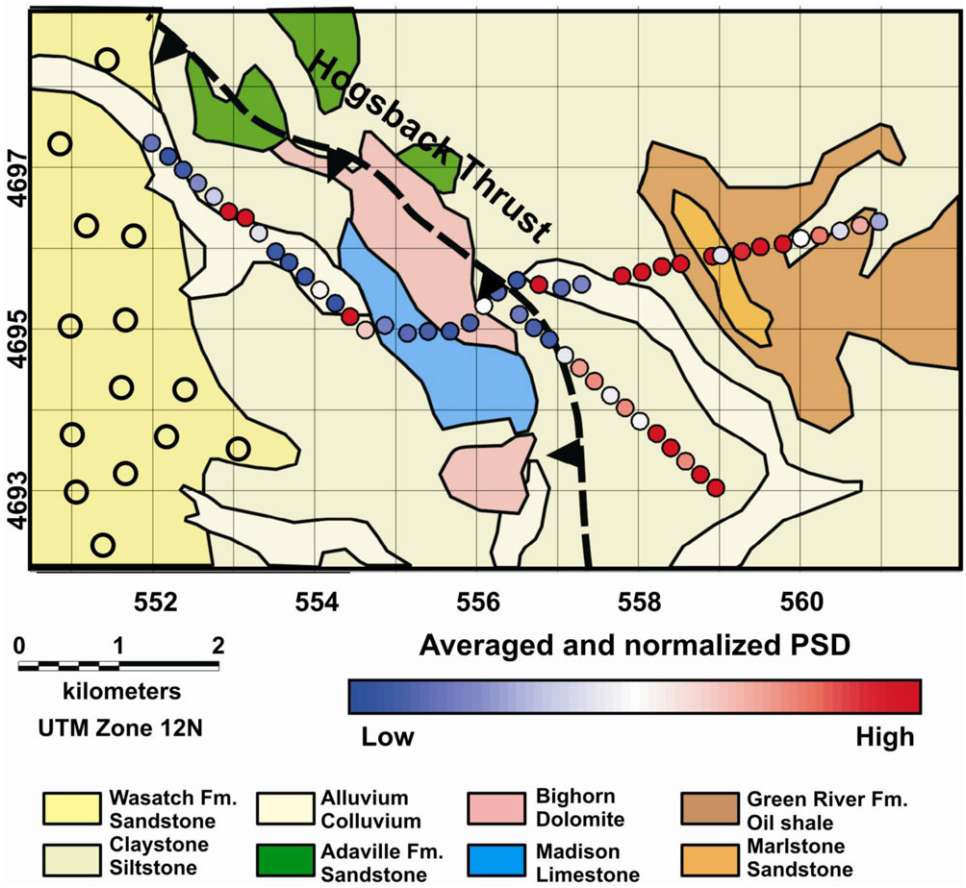

Figure 2 Geological map of the investigated area. Coloured circles show the averaged and normalized power spectral densities (PSD) at each station. See text for details. Labels of map axes are UTM coordinates in kilometres.

instruments and the consistency and the high-quality of the data set make it an ideal test ground to determine the value of ambient noise techniques (Saltzer *et al.* 2011). The crustal structure beneath the experiment is constrained by local well control and other active and passive studies. The dominant structural feature is the Hogsback Thrust, where paleozoic carbonates overly clastic sediments. The thrust reaches the surface at the eastern edge of the Cretaceous Mountain and is predominantly oriented north-south. East of the thrust, clastic sediments (clay stone and silt stone) are exposed. The Wyoming state highway 235 runs parallel and west of a prominent mesa, which comprises oil shale and sand stone. A schematic of the surface geology is provided in Fig. 2.

The major goal of our study is the evaluation of the applicability of seismic interferometry from locally generated ambient noise for shallow subsurface characterization. We test and adapt different algorithms that are routinely used in global and regional surface wave studies and aim at defining differences in application and parameter selection. Although we address the entire seismic exploration community, in particular practitioners of passive seismology and interferometry should find useful information in this case study.

Section 2 introduces the data set. In Section 3, we review the basic concepts of seismic interferometry, outline our processing approach and analyse the effect of different processing parameters. The optimum algorithms and parameters are then applied to the entire data set to derive a substantial set of interferograms, which also allow identifying the noise source. The interferograms are inverted for shallow surface wave velocities in section 4 and section 5 concludes with the most important insights and recommendations for further deployments and studies.

2 DATA

Analysis of the raw data focused on the calculation of power spectral densities to obtain an initial estimate of the exploitable frequency content. We found signals over a wide

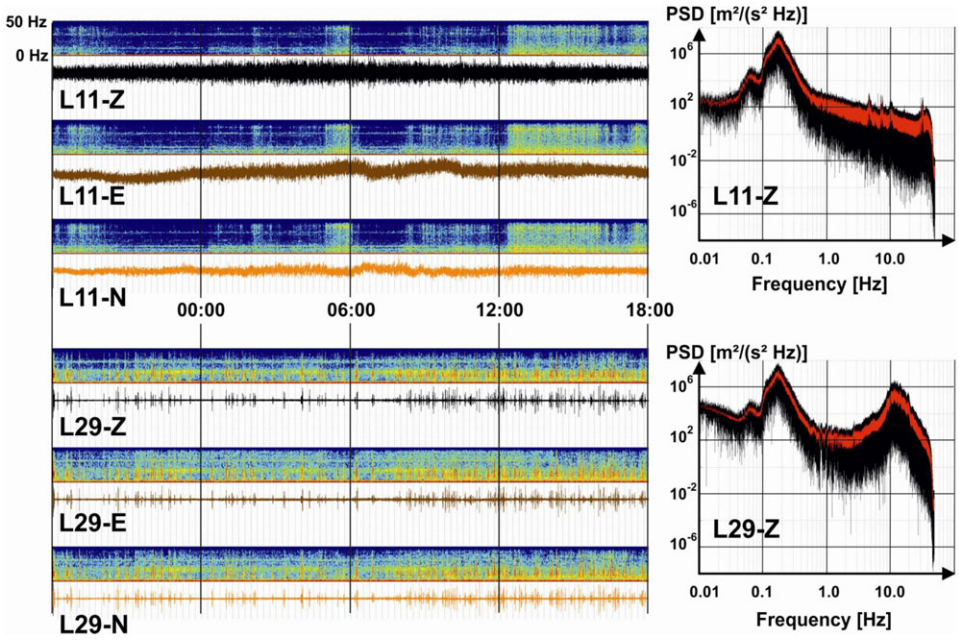

Figure 3 Data, spectrograms and power spectral densities (PSD) of stations L11 and L29. The 24 h long data series start at November 29th, 2008 at 18:00 local time. The red curve in the PSD plots is a running average over 10 samples.

frequency range, sometimes up to the Nyquist frequency (50 Hz). Figure 3 gives an example of the two stations L11 and L29 where the latter one is at a close proximity to the road. L11 shows the onset of an unknown noise activity at 12:30 local time. The pronounced noise bursts at station L29 are attributed to passing cars or trucks but their high-frequency contributions decay quickly with the distance to the road. The earth's microseism, peaking between 0.05–0.5 Hz (Webb 1998) can be clearly seen on all stations. These signals are excited by interactions between ocean waves and the ocean floor. Our investigation shows a broad variation on both spatial and temporal scales, though a complete and detailed analysis of the spectral characteristics of the entire data set is beyond the scope of this paper.

The uniform instrumentation allowed for a direct comparison of the power spectral densities (Fig. 2) for the entire observation period of 7 months. The coloured circles in Fig. 2 represent the average power spectral density of the vertical component of each station. These values are obtained as follows. First, the averages of the power spectral densities within certain frequency bins (0.001–0.1, 0.1–0.3, 0.3–1, 1–5, 5–10, 10–20, 20–40 Hz) are calculated for each 24 hour interval within the entire observation period. In each frequency bin, averaging is performed a second time over all 24 hour intervals and these double-averaged values are then normalized to the maximum and minimum of all stations. Finally, the shown values in Fig. 2 are calculated by averaging these normalized values over all frequency bins. Low values indicate a weak surface response and we found a clear large-scale correlation with surface geology since stations east of the Hogsback thrust show higher values. Outliers like the high values at two stations west of the thrust can be correlated with local machinery (e.g., pumping pads). Similar results were obtained for the horizontal components. If we further restrict the data to time windows, which include surface and body waves from regional and global earthquakes only, we derive the same pattern. We therefore interpret these values as indicators for local attenuation due to the near-surface geological structure. A detailed treatment is beyond the scope of this study but we conclude that some stations will be more affected by attenuation and thus might anticipate interferograms of lower quality west of the Hogsback thrust.

3 PROCESSING

3.1 The virtual source method and the stationary phase principle

In seismology, a Green's function represents the impulse response of the earth. The virtual source method (Bakulin and Calvert 2006) aims to derive a Green's function between two receiver stations by transforming one station into a (virtual)

seismic source. It is assumed that one or more (real) sources radiate seismic energy that is recorded by a set of receivers. As our study is based on seismic noise of initially unknown origin, we refer to those real sources as 'noise sources'. The noise sources are assumed to be located outside the deployment. In case of ambient noise studies (e.g., Wapenaar and Fokkema 2006) and continuous recording, the timing and location of the noise sources do not have to be known, provided they are uniformly distributed. By correlating trace $\mathbf{y}_A(t)$ at receiver A (the virtual source) with trace $\mathbf{y}_B(t)$ at receiver B, the interferogram $\mathbf{g}_{AB}(t)$ between the two instruments is obtained:

$$\mathbf{g}_{AB}(t) = \mathbf{y}_B(t) \times \mathbf{y}_A(t) = \mathbf{y}_B(t) * \mathbf{y}_A(-t) \tag{1}$$

Note that we consider the traces and thus the Green's function as time series of discrete samples, which are represented as vectors. In equation (1), the star sign denotes convolution that is equivalent to correlation with the reversed time series. For many reasons (e.g., source signature, instrument noise, attenuation, scattering phenomena, measurement of displacement instead of stress; Snieder 2007; Halliday and Curtis 2008; Tsai 2011), the obtained interferogram $\mathbf{g}_{AB}(t)$ is only an approximation to the actual Green's function and therefore an estimate of the impulse response of the earth. Thus Green's functions recovered by interferometry might be considered as empirical Green's functions.

Correlation results in both positive (causal) and negative (acausal) time lags. The character of the causal and acausal parts of the interferogram provides evidence on the noise sources: symmetry hints towards evenly distributed noise sources, while a stronger causal (or acausal) part indicates a dominance of noise sources closer to receiver A (or B) (Paul *et al.* 2005; Stehly, Campillo and Shaipiro 2006).

As correlation in the time domain is equivalent to convolution with the reversed time series, equation (1) can be stated in the Fourier domain as:

$$\mathbf{g}_{AB}(f) = \mathbf{y}_B(f)\overline{\mathbf{y}_A(f)}, \tag{2}$$

where the overbar denotes the complex conjugate.

Interferometry can also be approached in the Fourier domain by deconvolution (Snieder and Safak 2006; Vasconcelos and Snieder 2008; Wapenaar *et al.* 2010b):

$$\mathbf{g}_{AB}(f) = \mathbf{y}_B(f)/\mathbf{y}_A(f). \tag{3}$$

Equation (3) can also be written as:

$$\mathbf{g}_{AB}(f) = (\mathbf{y}_B(f)\overline{\mathbf{y}_A(f)})/||\mathbf{y}_A(f)||^2. \tag{4}$$

A modification to equation (4) leads to interferometry by cross-coherence (Aki 1957; Prieto, Lawrence and Beroza 2009; Wapenaar *et al.* 2010b):

$$\mathbf{g}_{AB}(f) = (\mathbf{y}_B(f)\overline{\mathbf{y}_A(f)})/(\mathbf{y}_B(f)\mathbf{y}_A(f)). \tag{5}$$

Equations (2), (4) and (5) are, apart from the denominator, identical, which in the two latter cases comprise the amplitude spectra of the seismic data. If the amplitude spectra are flat (unlikely in practice), the interferograms obtained by all three methods are of identical shape and recover identical empirical Green's functions. If not, each of the different Green's function recovery methods will result in different estimates of the impulse response of the earth. The performance of these three techniques is examined in more detail in section 3.3.

The stationary phase principle (Snieder 2004; Snieder, Wapenaar and Larner 2006) is of great importance to seismic interferometry. Translated to ray theory, it states that the dominant contribution to the reconstructed Green's function comes from raypaths that are identical prior to arrival at the receivers. Wapenaar *et al.* (2010a) showed that these paths are equivalent to rays that are parallel at the source. In case of a homogeneous half-space, the stationary phase region (location of the noise sources that satisfy the stationary phase principle) for surface waves is simply the outward extension of the line that connects the receiver and the virtual source.

In practice, seismic waves comprise finite frequencies and the raypath is replaced by the Fresnel zone (or finite-frequency kernel). Further, we may expect a multitude of noise sources distributed all over and around the investigated area. In this case, the stationary phase principle ensures a kinematically correct empirical Green's function if the noise sources are of equal strength and are distributed evenly around the virtual source-receiver pair. Only then will contributions from noise sources outside the stationary phase region cancel. The dominant contribution from oscillatory integrals where the phase varies much more rapidly than the amplitude comes from the integration points where the phase is stationary (section 6.5 of Bender and Orszag 1978 or section 2.7 of Bleistein 1984). For interferometric applications this implies that the dominant sources are those within the stationary phase region, provided the source strength varies over distance much more slowly than the phase of the interferometric integral does. The stationary phase principle is usually valid in global seismology because the dominant noise sources (ocean waves, strong earthquakes) are ubiquitous. At smaller scales, the noise sources may be concentrated at certain locations (e.g., cultural noise, roads, trees) and thus the results must be evaluated carefully

with respect to a possible violation of the requirement that noise sources are evenly distributed.

Coherent signals of noise sources may be expected to be of very small amplitude. Stacking of individual interferograms from different time windows is commonly applied to enhance information from ambient noise data. This increases the signal-to-noise (S/N) ratio of the interferograms by down-weighting non-coherent seismic energy.[1] Alternatively, correlation of the entire time series at once would be possible but computation is more efficient and practical when the continuous recordings are cut into short time windows. Correlation is then performed for each time window and the resulting individual interferograms are stacked into a final interferogram. The total amount of input data and the length of the time windows required depend on the virtual source-receiver distance, the subsurface structure (attenuation), the location, type and strength of the noise sources and on computational considerations. For the testing of processing parameters and methods (sections 3.2 and 3.3), we use 5 days of vertical component data (December 1st to December 5th of 2008) and cut them into 10 s time windows. A more exhaustive analysis of the time window length and the overall amount of data is presented in section 3.4.

3.2 Preprocessing

Prior to correlation, the data are subjected to a sequence of processing steps. Bensen *et al.* (2007) described data processing that is commonly applied to global-scale data (frequency filtering, temporal normalization, spectral whitening). We essentially followed their methodology but with some minor modifications as discussed below. The raw data indicate a broad spectrum (Fig. 3) that ranges from below the earth's microseism (0.07 and 0.13 Hz, respectively) to the Nyquyist frequency (50 Hz) but only spatially coherent signals will provide useful interferograms.

The exploration industry is interested in broadening the frequency content of seismic data towards the lower end of the spectrum to obtain improved starting models for full-waveform inversion (Sirgue and Pratt 2004; Denes, Starr and Kapoor 2009). For interferometric applications, the low-frequency threshold depends on the noise source, on the local subsurface structure and on the receiver spacing and aperture of the array. If the wavelength is large in comparison to the virtual source-receiver distance (e.g., earthquake surface waves), the correlation resembles a zero-lag peak. The same accounts for waves that arrive simultaneously at the receivers, e.g., vertical-incidence body waves from teleseismic earthquakes. Thus we exclude data that comprise surface and body waves from regional and global earthquakes, based on a catalogue by C. Byriol (pers. comm. 2011). Tests with different high-pass filters showed that a strong zero-lag arrival emerges if frequencies lower than 2 Hz are included. This may indicate that some earthquake energy is still remnant in the data set. Low-frequency oscillations of the basin, possibly excited by earthquake originated waves (e.g., Rial 1989), may also contribute. Because of their consideration we conclude that a high-pass filter of 2 Hz is required for further processing. With respect to the expected velocities of surface waves, 2 Hz is roughly equivalent to a wavelength range from 750–2000 m.

The high-frequency end of the spectral component that can be used is examined by different low-pass filters applied to the input data. Figure 4(a,c) shows interferograms obtained from correlation in the time domain applied to data band-pass filtered with different upper corner frequencies (20 Hz, 40 Hz). Both results appear noisy and do not give much additional insight into the subsurface structure. We further detect spurious energy over the entire frequency band (e.g., the zero-lag peak). This results from spectral whitening (see below) that, though applied after band-pass filtering, is automatically performed from the lowest to the Nyquist frequency. Analogously to active-source processing, we thus applied a band-pass filter after interferometry (post-stack filtering, Fig. 4b,d). It shows that the interferograms do not comprise coherent signals with frequencies higher than 5 Hz, no matter which low-pass filter is applied to the data. Note that the post-stack band-pass filter becomes obsolete if spectral whitening is performed over the same frequency range only as the prestack band-pass filter. This depends however on the actual implementation of the whitening algorithm. In our case, all shown interferograms are band-pass filtered from 2–6 Hz.

Though the stationary phase principle requires noise sources of equal strength, this is not generally the case; we therefore applied temporal normalization to the input data. Bensen *et al.* (2007) compared different algorithms and we additionally tested the performance of automatic gain control (AGC). The running-mean normalization by Bensen *et al.* (2007) is similar to AGC but is based on absolute amplitudes instead of squared amplitudes. We found the difference of

[1] Note that the term 'noise' is used throughout with two different meanings: prior to interferometry, it describes the ambient seismic energy that is radiated by the actual (real) sources. This noise is turned into a signal by interferometry, which creates a virtual seismic trace. Consequently, the S/N ratio of this trace (the interferogram) is high when the amount of ambient noise is high.

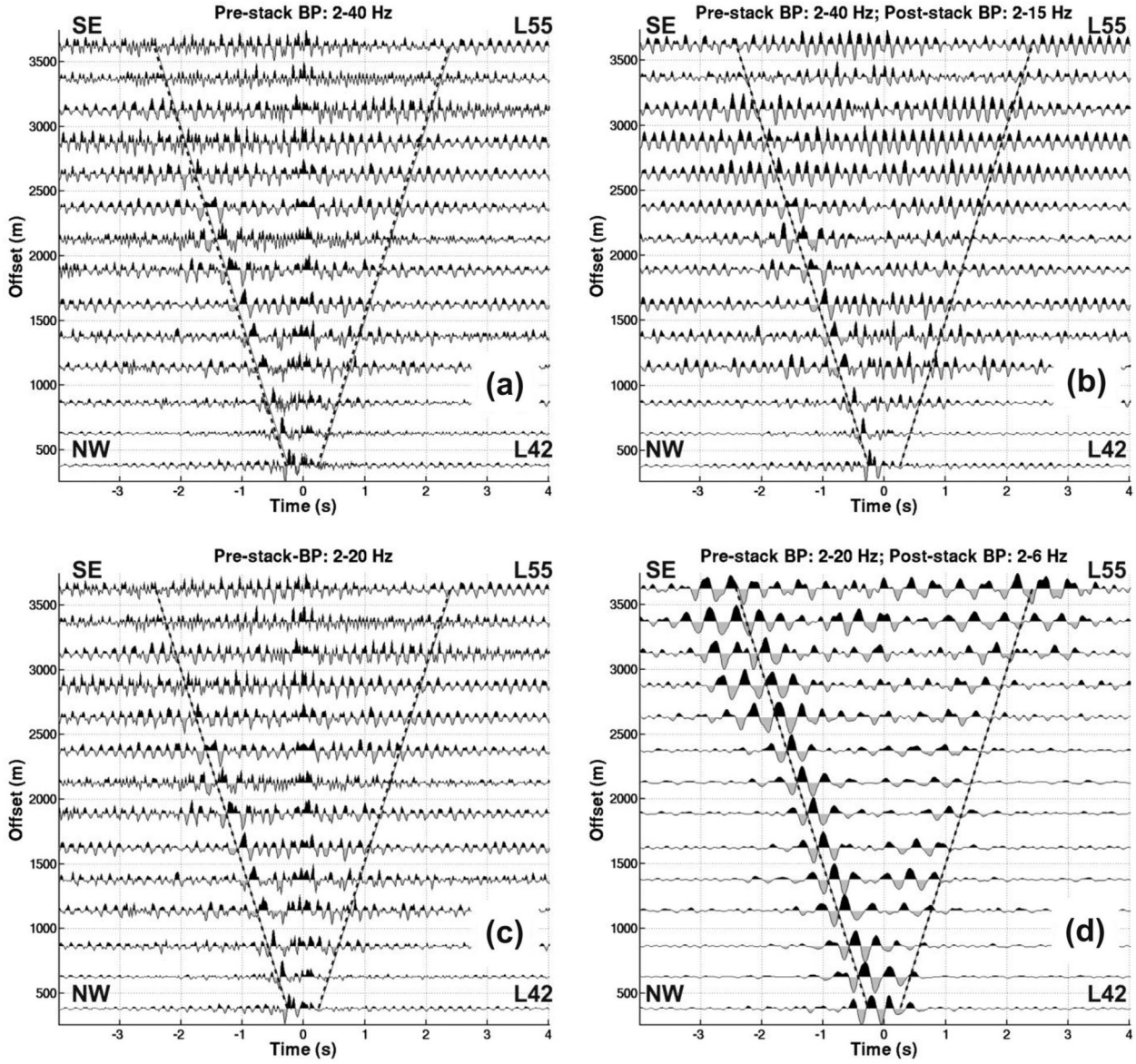

Figure 4 Comparison of different pre- and post-processing band-pass filters for virtual source L22 and receivers along segment 3. The broken lines indicate linear moveouts for a velocity of 1500 m/s. NW and SE refer to the geographic directions. See text for details.

one-bit normalization, running-mean normalization and AGC to be minor and finally chose the AGC operator with a window length of 0.1 s. One-bit normalization has the disadvantage of not being commutative with respect to rotation of the horizontal components, which is needed for the transformation to radial and transverse components (cf. section 3.5).

Spectral whitening aims at normalizing the amplitude spectrum of the input data, thus boosting low-amplitude frequency components and collapsing monochromatic signals. The latter is of importance in industrial settings, since industrial machinery (e.g., drill rigs, pumps) operate at discrete frequencies (e.g., Poletto and Miranda 2004). Total whitening may be performed by normalizing the amplitude spectra at all frequencies. User-controlled whitening is achieved when the amplitude spectrum is divided by a smoothed version of itself (Bensen *et al.* 2007). A strong smoothing filter (smoothing over large frequency intervals) has little effect compared to weak smoothing (smoothing over small frequency intervals). We prefer user-controlled smoothing since total whitening results in slightly more spiky interferograms. Tests show that

the optimum smoothing length with regard to the S/N ratio of the interferograms is 0.1 Hz. Like one-bit normalization, total whitening is also not compatible with the transformation to radial and transverse components (section 3.5). Because spectral whitening introduces incoherent high-frequency artefacts, post-processing (after interferometry) always included a band-pass filter of 2–6 Hz and weighted smoothing in the time domain with a window length of 0.3 s. The linear moveout of the arrivals is a prominent feature and an indication for surface waves (Fig. 4d).

3.3 Comparison of different algorithms

As outlined in section 3.1, the three different interferometry algorithms (correlation, deconvolution, cross-coherence) are identical if the amplitude spectra of the input data are flat. The flatness depends on the whitening operator (section 3.2) and as we chose user-controlled whitening, different results are expected. It is noted that both deconvolution and cross-coherence intrinsically whiten the data by spectral division, although the whitening operator (the denominator in equations (3–5)) varies with virtual source and receiver stations. E.g., spectral notches that are stronger at the receiver station than at the virtual source will not be completely removed. For these reasons and for simplicity and consistency, we applied all three methods on a uniform, pre-whitened data set.

The comparison is shown in Figs 5 and 6. For short offsets (< 2 km; Fig. 5), the results are similar. At medium offsets (2–4 km; Fig. 6), the correlation interferograms are generally more noisy, in particular if whitening is weak. This difference with deconvolution and cross-coherence might be explained by the additional spectral division (equations (3–5)), which additionally equalizes the receiver and virtual source amplitude spectrum. Cross-coherence and in particular deconvolution, exhibit a pronounced zero-lag peak at medium offsets, which is slightly enhanced in the case of weak whitening. A similar behaviour is observed at offsets larger than 4 km. In case of weak whitening and correlation, monochromatic signals persist in the interferograms. Ultimately, theoretical equivalence results in the fact that the choice of method will be determined by the character of the data set of interest and the preference and expertise of the analyst. In this case, we find that the best results are achieved with strong whitening (smoothing over 0.1 Hz wide frequency intervals) and by the use of cross-coherence. Consequently, all following computations are performed with this combination.

3.4 Influence of the window length and number of input data

In case of continuous recordings and unknown noise sources, the choice for the amount of input data is important. Depending on the available data and computing resources, different strategies can be imagined. In the case of a short, temporary deployment, overlapping time windows may be used to increase the probability of correlating signals from noise sources (Seats, Lawrence and Prieto 2012). For our data set, we regard the 7 months of data to be sufficiently long and therefore use adjacent time windows and restrict the analysis to the number and length of the time windows.

The wave forms in Figs 4–6 are based on 10 s long time windows from a 5 day period. In the first test, the 5 day period is extended to 10, 15, 20 and 35 days and also decreased to 1 day. In case of short to medium offsets and low attenuation, there is no direct correlation of the S/N ratio of the interferogram with the length of the observation period. Instead it turns out that the interferograms from the individual 5 day periods differ significantly, which indicates varying strength of the noise source within these time frames. The same effect is observed at large offsets and/or stations located in regions of stronger geological attenuation (e.g., section 1). In order to improve the S/N ratio, a possible strategy would be the selection and stacking of interferograms from periods with a higher S/N ratio.

The second test is a variation of the length of the time windows (10 s, 20 s, 60 s, 120 s). Longer time windows provide clearer surface wave arrivals and in particular the zero-lag peak (section 3.3) is minimized. A possible explanation for both observations is the dissection of long coherent signals by cutting the input data into short time windows. The zero-lag peaks, which are considered as artefacts from remnant unwanted energy (e.g., high-frequency body waves of earthquakes not included in the used catalogue, section 3.2), are down-weighted by improved correlation of longer time series. With regard to these tests, all the following computations are performed for 120 s long time windows from a 5 day period (December 1st to December 5th, 2008).

3.5 Horizontal component processing

As the horizontal component data (east – E, north – N) are of similar quality as the vertical (Z) component data, we also calculated interferograms for the horizontal components. On average, initial tests showed clear arrivals at the (N)-interferograms and a lower S/N ratio at the

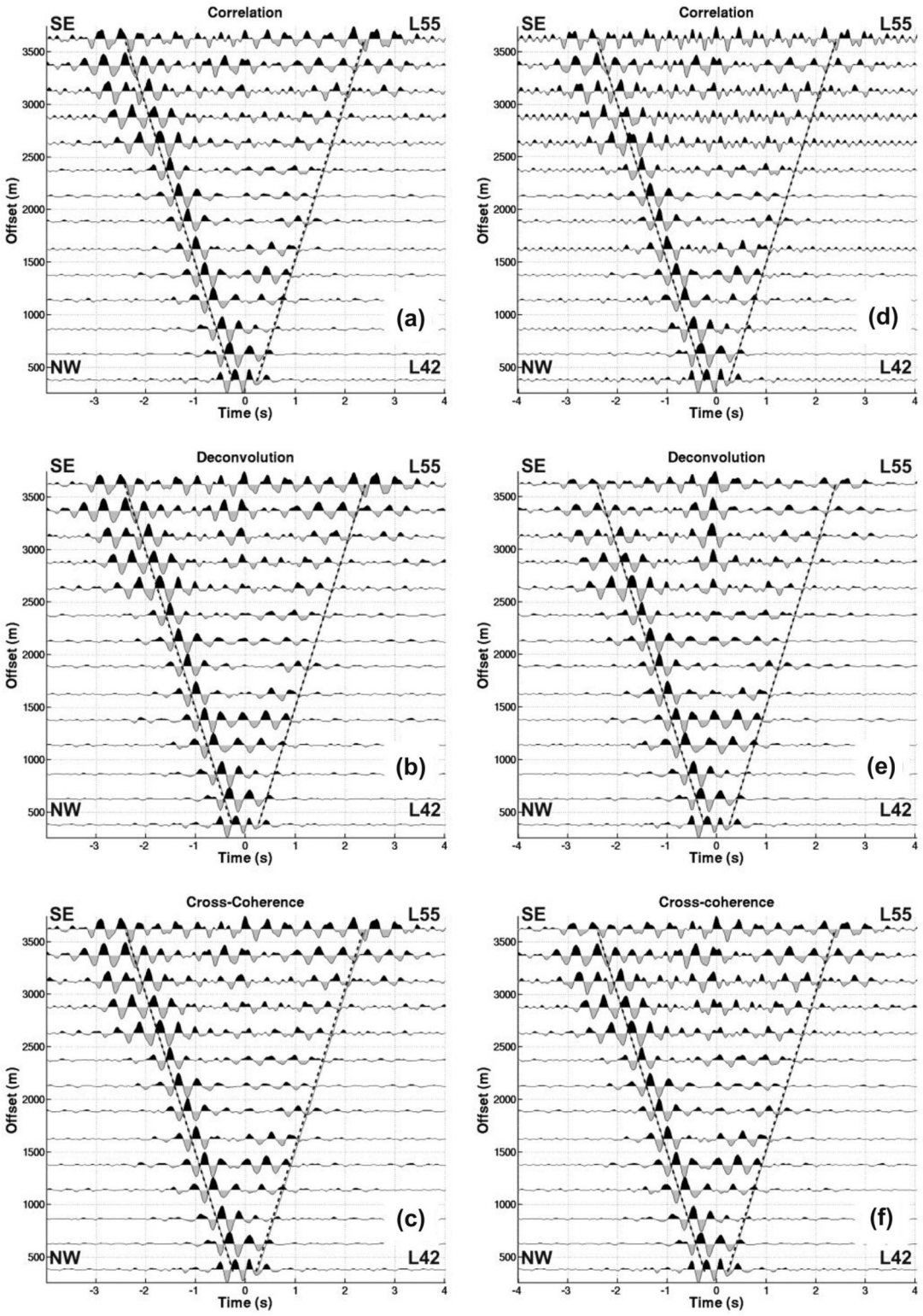

Figure 5 Comparison of correlation (a,d), deconvolution (b,e) and cross-coherence (c,f) for virtual source L22 and receivers along segment 3 (short to medium offsets). The left/right columns (a–c/d–e) are based on strongly/weakly whitened data (smoothing interval 0.1 Hz / 1 Hz). The broken lines indicate linear moveouts for a velocity of 1500 m/s.

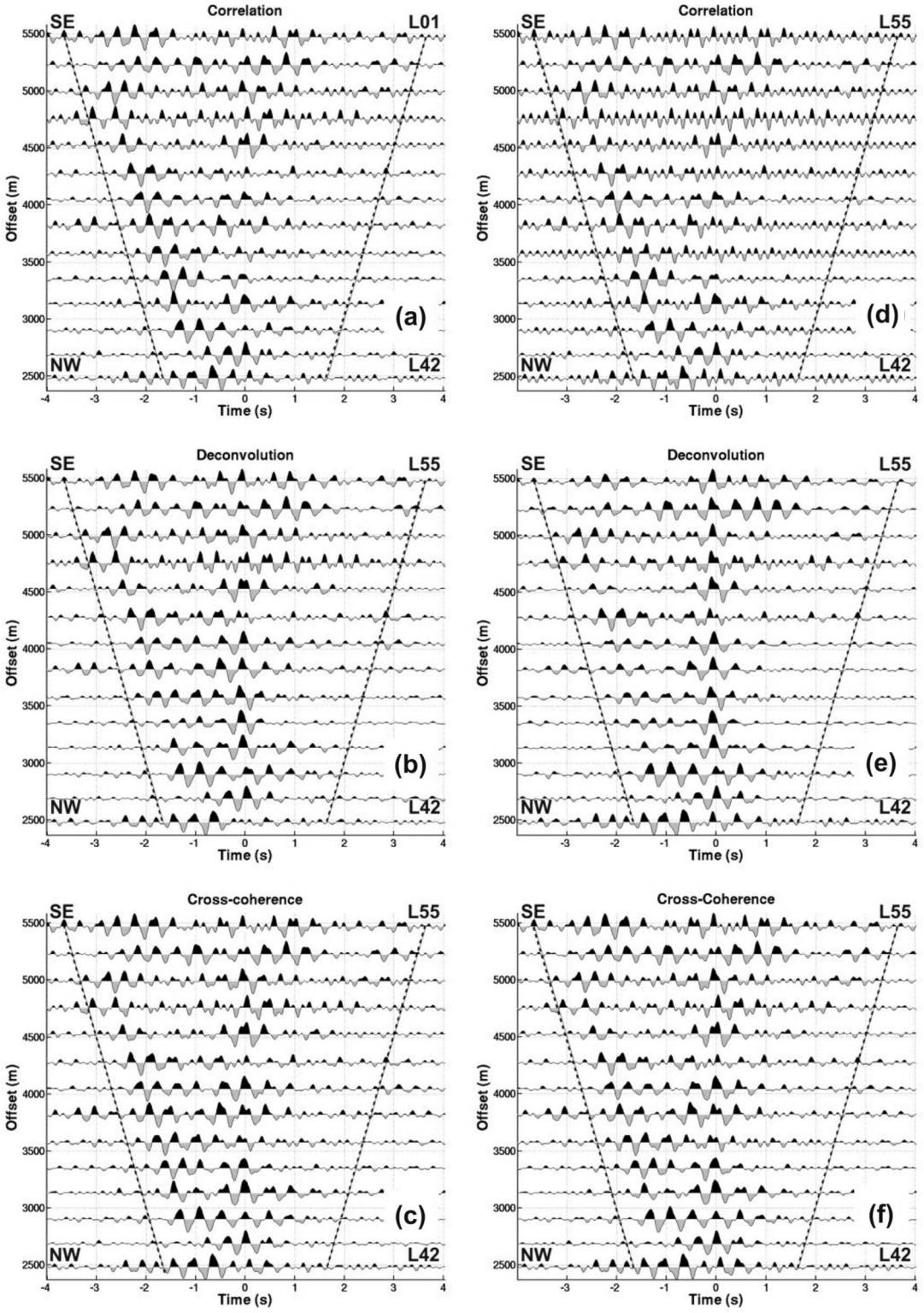

Figure 6 Comparison of correlation (a,d), deconvolution (b,e) and cross-coherence (c,f) for virtual source L12 and receivers along segment 3 (medium to long offsets). The left/right columns (a–c/d–e) are based on strongly/weakly whitened data (smoothing interval 0.1 Hz / 1 Hz). The broken lines indicate linear moveouts for a velocity of 1500 m/s.

(E)-interferograms. Further, most of the (N)-interferograms exhibit significantly higher apparent velocities, which might indicate the presence of faster Love waves. We analysed this by the transformation of the horizontal (E,N) components into the radial and transverse (R,T) components.

The radial direction is defined as the virtual source – receiver azimuth α and the transverse direction points 90 degrees clockwise to the radial direction. In case of a layered structure, the radial component (R) and the vertical component (Z) should highlight the Rayleigh wave, while the Love wave should be present on the transverse (T) component only. Surface waves reconstructed by interferometry suffer the loss of their original particle motion due to the correlation process, thus the 90° phase shift between the vertical and horizontal components of the Rayleigh wave cannot be observed from (Z)- and (R)-interferograms. The phase shift may be detected by comparing (Z)-interferograms with (Z-R)-correlations but Rayleigh and Love waves can also be separated by their different velocities. Lin, Moschetti and Ritzwoller (2007) analysed the radial and transverse parts of crustal seismology interferograms and were able to demonstrate that the T-component has a higher S/N ratio than the R-component and that the Love wave is clearly present on the T-component. Subsequently they derived Rayleigh wave velocities from Z-component readings and Love wave velocities from T-components. We might expect the same but have to consider that the scale of local velocity variations with respect to the wavelength is different than in crustal seismology. Local wave front curvatures at the stations will be larger and Love and Rayleigh waves will be partially projected on both the (R) and (T) components. Consequently, the wave separation by (R,T) transformation is less effective. Additionally, due to the short offsets Rayleigh and Love waves are more likely to interfere, which hampers their separation.

Preprocessing becomes an issue in case of (R,T) transformation. Ideally, one would perform rotation of the raw data first, then preprocessing and finally apply interferometry. This is not practical with a 3D deployment because for each virtual source the azimuth α depends on the receiver in question and preprocessing must be performed for each virtual source-receiver combination with an according multiplicative effect on the computational expense. Like Lin *et al.* (2007), we overcame this by choosing preprocessing operators that are commutative with the rotation operator such that preprocessing has to be applied to the horizontal component raw data ($\mathbf{e}(t)$, $\mathbf{n}(t)$) only once.

Band-pass filtering and whitening can be regarded as convolution operators in the time domain. Commutativity is achieved if the convolution operators for both components are identical, which is the case for a band-pass filter with constant corner frequencies. In case of user-controlled whitening (section 3.2), a practical solution is achieved by averaging the smoothed amplitude spectra of both components. Temporal normalization (AGC) is approached in a similar way. AGC can be formulated as an element-wise multiplication of the raw data series ($\mathbf{e}(t)$, $\mathbf{n}(t)$) with series of normalizing factors ($\mathbf{g}_e(t)$, $\mathbf{g}_n(t)$). Again, commutativity is satisfied when $\mathbf{g}_e(t)$ and $\mathbf{g}_n(t)$ are identical. As the normalizing factors depend on the data, we calculate both $\mathbf{g}_e(t)$ and $\mathbf{g}_n(t)$ and choose the smaller one for each sample. One-bit normalization cannot be adapted in a similar fashion and thus it is not commutative with rotation. With regard to their subsequent workflow, Lin *et al.* (2007) applied interferometry on preprocessed data and finally rotated the interferograms. For reasons related to data handling, we switch this order and perform the rotation of the preprocessed data before applying interferometry.

The parameters for the preprocessing steps (band-pass corner frequencies, AGC window length and whitening smoothing length) for the horizontal components are identical to the ones used for vertical-component processing. A comparison of all five components (Z, N, E, R, T) is shown in Figs 7 and 8, where the spacing of the traces is proportional to their virtual source-receiver azimuth. Figure 7 gives an example where the virtual source is west of the receivers and the state road is east of the receivers. We expect that this road is the dominant noise source (cf. section 3.6), which is also illustrated by the appearance of waves in the acausal part only. Therefore the faster Love waves would not only be expected on the T-component (Fig. 7f) but also mainly on the N-component (Fig. 7c) at W-E oriented azimuths. Due to the sine and cosine functions in the rotation operator, the contribution of the N-component is still twice as large as from the E-component (Fig. 7b) at an azimuth of 115°, which explains the overall similarity of the T- and N-components (Fig. 7c,f). Comparing the Z-, R- and T-components, the latter ones feature a higher apparent velocity, which is interpreted as the Love wave.

Figure 8 shows that Love and Rayleigh waves might also be associated with different excitations. As the virtual source and the southernmost receivers are located close to the road, both causal and acausal signals may be expected at these receivers. This is the case for the Z- and R-components (Fig. 8d,e) but the causal signals are missing at the T-component (Fig. 8f). We therefore conclude that stronger Love waves are generated at the southern part of the road.

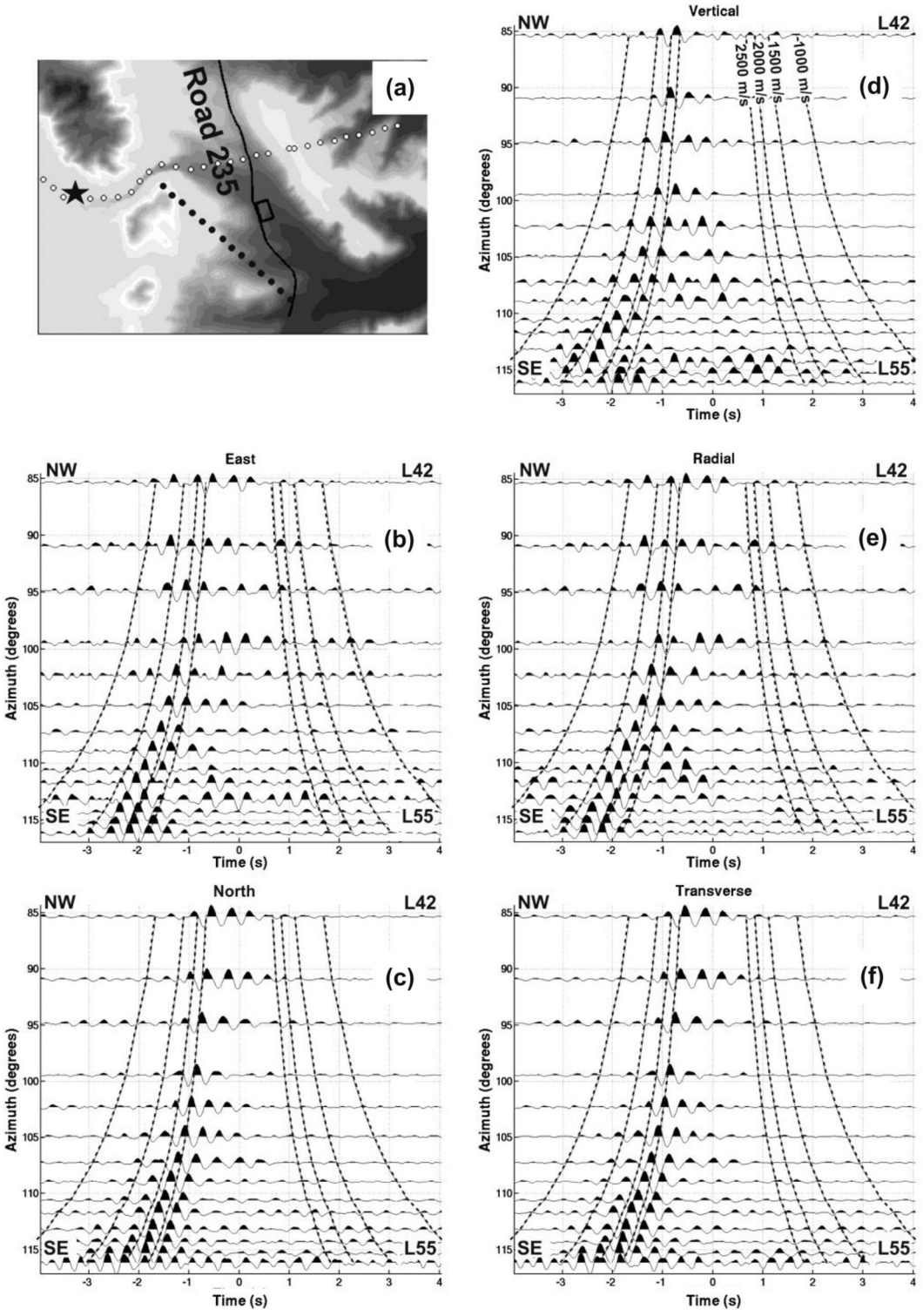

Figure 7 Transformation of the east (b) and north (c) components to radial (e) and transverse (f) components for virtual source L16 (star in (a)) and receivers along segment 3 (black dots in (a)). Trace spacing is proportional to the virtual source – receiver azimuth. The broken lines indicate linear moveouts for different velocities. The azimuth is counted positive in clockwise direction starting from the north axis.

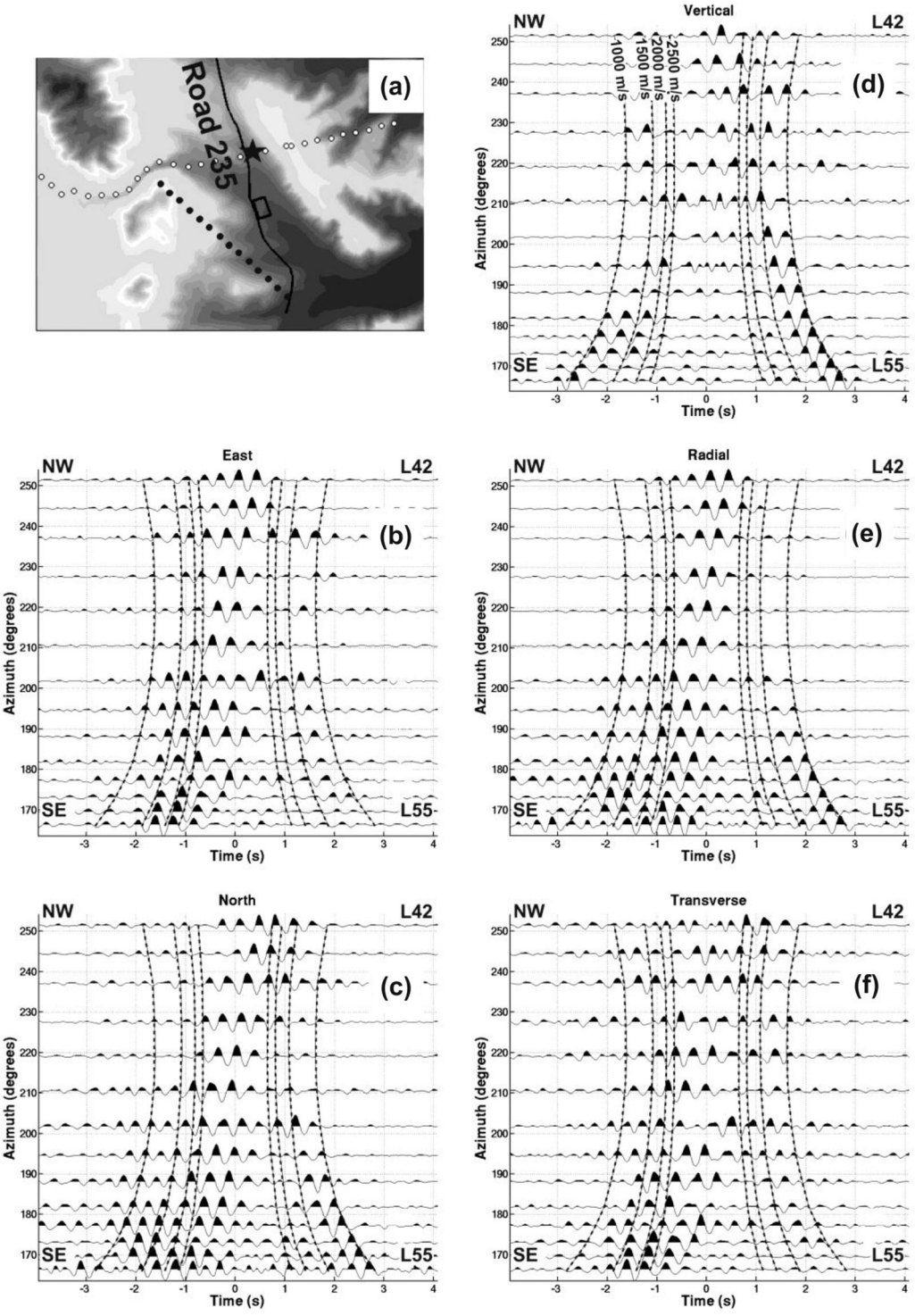

Figure 8 Transformation of the east (b) and north (c) components to radial (e) and transverse (f) components for virtual source L30 (star in (a)) and receivers along segment 3 (black dots in (a)). Trace spacing is proportional to the source – receiver azimuth. The broken lines indicate linear moveouts for different velocities.

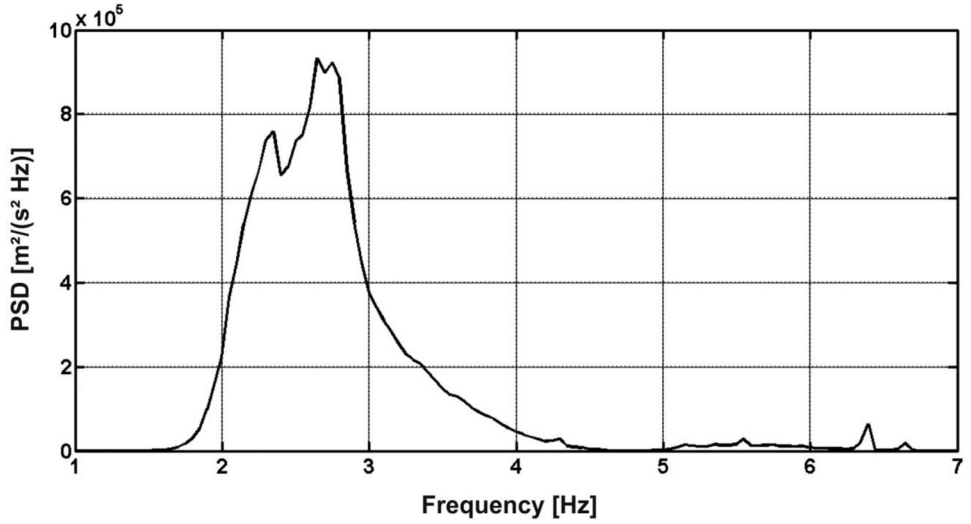

Figure 9 Stacked power spectral density of all obtained interferograms. See text for details.

3.6 Results

Splitting the 5-day interval (December 1st to December 5th, 2008) into 120 s long windows results in 3600 data sections for each of the three components. For 2916 virtual source-receiver pairs, the total number of all calculated individual interferograms amounts to approximately 31 000 000. In this section we draw conclusions on the obtained final interferograms, in particular with respect to the frequency content and the noise source. Due to the large number of interferograms, emphasis is laid upon exemplary and summative illustrations.

Overall, the comparison between the three components suggests the presence of both Rayleigh and Love waves due to their different apparent velocities. Surface waves appear clearer on Z- and T-components than on R-components. The derived waveforms have a strong amplitude and high S/N ratio. Nevertheless, the arrivals are not always characterized by one pronounced peak but often by a sequence of two, three, or more peaks of similar amplitude (e.g., Figs 5–8). This is a consequence of the narrow frequency spectrum (Fig. 9). A closer inspection shows that the maxima at 2.3 Hz and 2.8 Hz are differently pronounced on the vertical and horizontal components. Thus they are related to a slightly varying frequency response of the vertical and horizontal component instruments. Overall, the narrow band prevents the extraction of dispersion properties (cf. section 4). Frequency-wavenumber analysis is hampered by the limited spatial sampling and could only be used to obtain rough and approximate phase velocities, which however can also be obtained from the interferograms in the time domain.

The individual peaks in the interferograms can be correlated but the true onset of the arrivals is not always clear. Thus the envelope function (modulus of the analytical signal) is applied in order to reduce the wavelet to a single peak. The envelope function is additionally raised to its 5th power to enhance the strongest amplitude, which mostly corresponds to the surface wave arrival (Fig. 10). This procedure retains the kinematic properties of the observed wave and the transformed wavelet now represents group velocities instead of phase velocities. The envelope calculation of the horizontal components may be flawed at short offsets, where Love and Rayleigh waves are superimposed. Also, non-stationary contributions will result in inaccuracies but overall the analyst can pick arrivals much more consistently than prior to the envelope calculation.

To obtain a more representative picture of the investigated area, we stack a sub-set of the final interferograms into offset bins with a size of 100 m. Due to local velocity variations, we have to expect to mix phases with different arrival times in each bin and thus velocity information deduced from the stacks must be interpreted with caution. The data subset is defined by the stations L12–L31 and L42–L55, which feature interferograms with the clearest appearance. Since the moveout and the spacing of the stations are too large with respect to the wavelength, we stack the Hilbert transformed data. The results for all three components are shown in Fig. 11. Arrivals on the T-component have a higher apparent velocity and these arrivals can be observed over longer offsets. Z- and R-component arrivals appear rather similar, with an overall

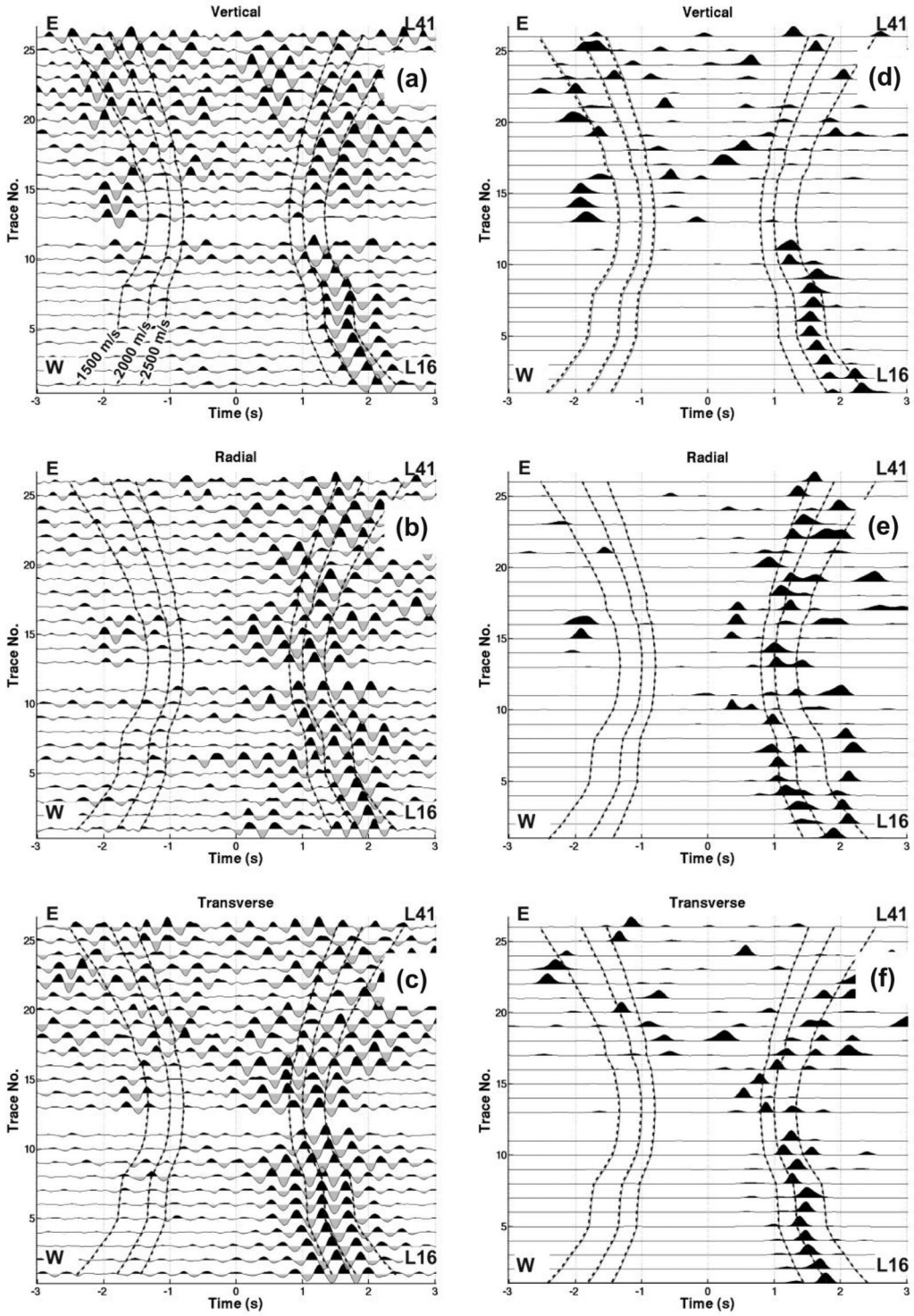

Figure 10 Interferograms of the vertical (a,d), radial (b,e) and transverse (c,f) components for virtual source L51 along segment 2. The trace spacing is equidistant. The right column (d–f) shows the application of the Hilbert transform. The broken lines indicate linear moveouts for different velocities.

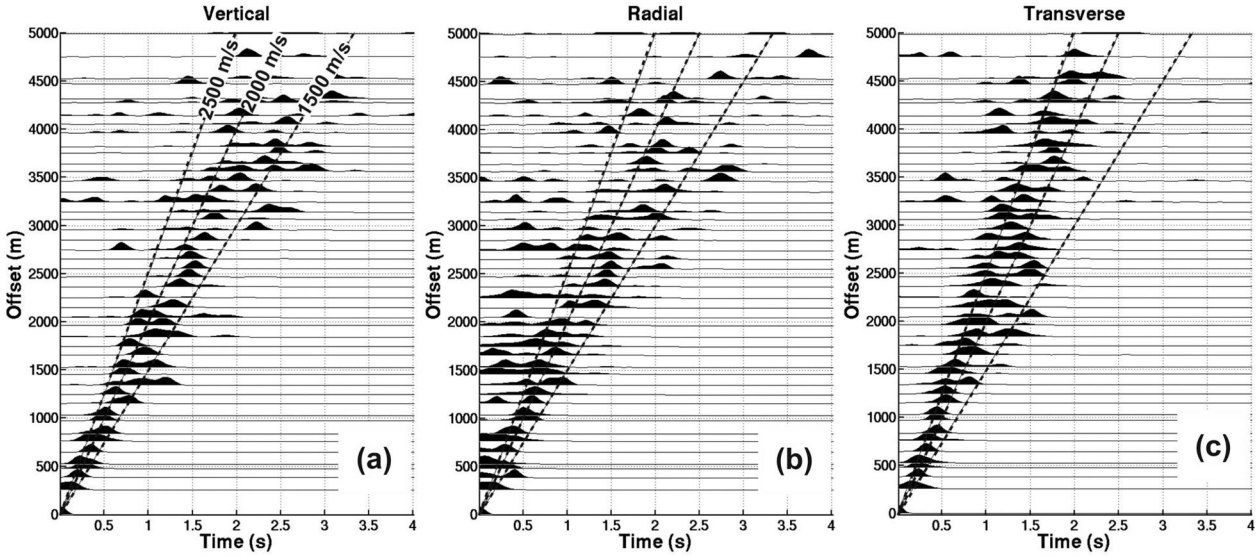

Figure 11 Common offset stacking applied to a subset of Hilbert-transformed interferograms (see text for details). The broken lines indicate linear moveouts for different velocities. (a,b,c): vertical, radial and transverse component data, respectively.

lower S/N ratio of the R-components. This observation was also made by Lin *et al.* (2008), although they analysed data on a global scale. The higher S/N ratio on the Z-component in comparison to the R-component may be related to the subsurface structure (e.g., Boore and Toksöz 1969). Overall, the common offset stacks strengthen the assumption that both Rayleigh and Love waves are observed.

Overall we obtain a substantial set of useful interferograms, both on in-line and cross-line virtual source-receiver pairs, which indicates a wide distribution of stationary source points. The examples shown so far feature a pronounced difference of the causal and acausal parts. This is observed throughout the area, where on average the acausal part dominates. Note that the westernmost stations (L01–L11) exhibit a lower S/N ratio. For virtual sources located west of the state road, receivers at and east of the mesa (L32–L41) show only little coherent energy and observed surface waves often arrive with unreasonably high velocities. The latter observation could be explained by the existence of a dominant noise source located in-between virtual sources and receivers. Altogether, there is strong evidence for a dominant noise source in the eastern part of the deployment and we conclude that traffic from the state road 235 excites the majority of the observed surface waves.

The observed variability of the quality of the interferograms with respect to the used time frame (section 3.4) might also be explained by irregular traffic activity. With respect to the geometry of the deployment, the north-south oriented road provides a large number of stationary source points. Lak, Degrande and Lombaert (2011) analysed the frequency response of roads to traffic by taking into account the construction of the road, the type of vehicle and the soil structure. They focused on the near-field effect (2–64 m) and concluded that the resulting spectrum mainly depends on the eigenfrequencies of the vehicles that range from 2–15 Hz. Since the offsets in our study are much larger, we expect to observe only the lower end of this spectrum.

4 INVERSION

The inversion of surface waves for depth-dependent shear-wave velocities is a standard procedure for global surface wave data. The frequency-time analysis method (FTAN; Dziewonski, Bloch and Landesmann 1969; Levshin *et al.* 1989) makes use of the dispersion characteristics of surface waves and is commonly applied to Rayleigh waves (Bensen *et al.* 2007 and references therein) and also to Love waves (Lin *et al.* 2008). FTAN provides dispersion curves for group velocities for a single source – receiver combination. The surface wave velocity-frequency relation is inverted for an average shear-wave velocity-depth relation between the source and receiver. We also applied FTAN to interferograms but due to the limited bandwidth in conjunction with the lateral geological variability we did not derive meaningful dispersion curves.

On the other hand, we derived a substantial number of useful interferograms on both in-line and cross-line virtual

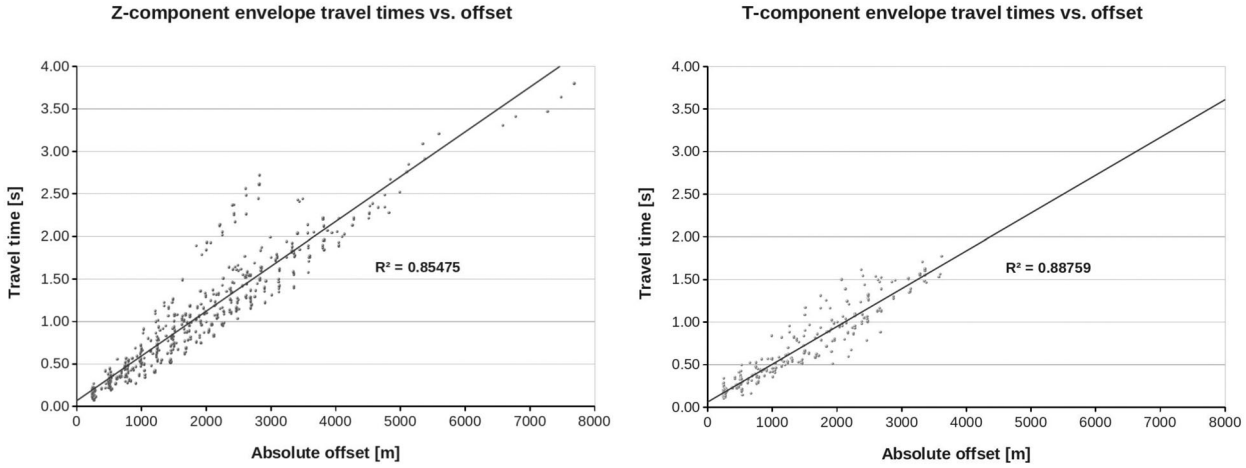

Figure 12 Picked surface wave traveltimes versus offset for Hilbert-transformed interferograms of the Z- and T-components. The slopes of the regression lines correspond to 1880 m/s and 2250 m/s, respectively. The zero-offset times are in the order of +0.05 s and are attributed to the entire post-processing steps including the Hilbert transform. They are subtracted from the traveltimes prior to the inversion.

source-receiver combinations. The envelope calculation facilitates consistent manual picking of surface wave arrival times. Consequently, these arrival times can be inverted for laterally varying group velocities by a tomographic approach similar to the simultaneous iterative reconstruction technique (SIRT; e.g., van der Sluis and van der Horst 1987). Modifications of the SIRT method for lateral velocity modelling are given by Iwasaki (2002), Song *et al.* (2004) and Behm *et al.* (2007). We parametrized the surface velocities at grid points with a lateral spacing of 250 m. Surface wave paths are approximated by straight rays between the virtual source and the receiver. We are aware that these simplifications may introduce artefacts in the obtained models but we consider them to be of equal or minor effect in comparison to the accuracy of traveltime picking.

If the surface velocity at a grid point is expressed as the slowness s, the traveltime t for a specific ray is calculated from:

$$t = \sum_{i=1}^{N} l_i \sum_{j=1}^{M} \lambda_j s_j. \quad (6)$$

The ray is split into N segments of equal length l_i, where N is the ratio of the total ray length (offset) to the grid point spacing (250 m). The corresponding slowness for each segment is represented by the second summation term in equation (6) and it is interpolated from the slownesses s_j at the neighbouring grid points. λ_j is a factor that decreases with the distance between the ray segment midpoint and the j-th grid point. The number M of contributing grid points is defined by a maximum distance of 375 m. The λ_j are calculated from a distance-dependent Gaussian function to guarantee smooth behaviour for the velocity interpolation and they are normalized such that their sum is 1.

For all observed traveltimes t_{obs}, a set of linear equations is established and solved for the unknown slownesses s_j at the grid points. Traveltime residuals of an initial model are calculated and singular value decomposition (SVD) is used for the inversion. The trade-off between the RMS error of the traveltime residuals and the variance of the derived velocity map is controlled by a cut-off value for the eigenvalues and additional smoothing of the obtained slowness improvements.

At this stage we focus on the large-scale structure of the region, which is more sensitive to systematic mispicks (e.g., following a wrong phase) than to slightly inaccurate traveltime readings. Correlation-based traveltime picking improves the accuracy of individual picks but nonetheless a visual control is necessary to check for systematic mispicks. We therefore chose to pick traveltimes manually. Traveltimes are only picked if the phases can be clearly correlated over at least two adjacent stations. Additional quality criteria are the S/N ratio and a realistic apparent velocity (1000–3000 m/s). These envelope traveltimes (Fig. 12) are inverted for group velocities, where vertical-component data provide Rayleigh wave velocities and transverse-component data provide Love wave velocities. We chose constant velocity initial models and calculated the velocities from the slope of the regression lines in Fig. 12. Picks are limited to traces with offsets between 0.3–5 km. The inversion statistics are summarized in Table 1.

Table 1 Statistics and results for the inversion of envelope traveltimes.

Type	no. of traveltime picks	initial velocity [m/s]	Traveltime residual RMS prior to the inversion [s]	Traveltime residual RMS after the inversion [s]	average / std.dev/ min / max of the velocities after the inversion [m/s]
Z-component	634	1880	0.272	0.117	1757 / 325 / 1104 / 2373
T-component	247	2250	0.154	0.109	2179 / 256 / 1545 / 2618

Table 2 Statistics and results for the inversion of traveltime differences.

Type	no. of traveltime differences	Traveltime residual RMS prior to the inversion [s]	Traveltime residual RMS after the inversion [s]	average / std.dev/ min / max of the velocities after the inversion [m/s]
Z-component	643	0.046	0.052	1809 / 369 / 1122 / 2624
T-component	465	0.027	0.026	2107 / 261 / 1636 / 2619

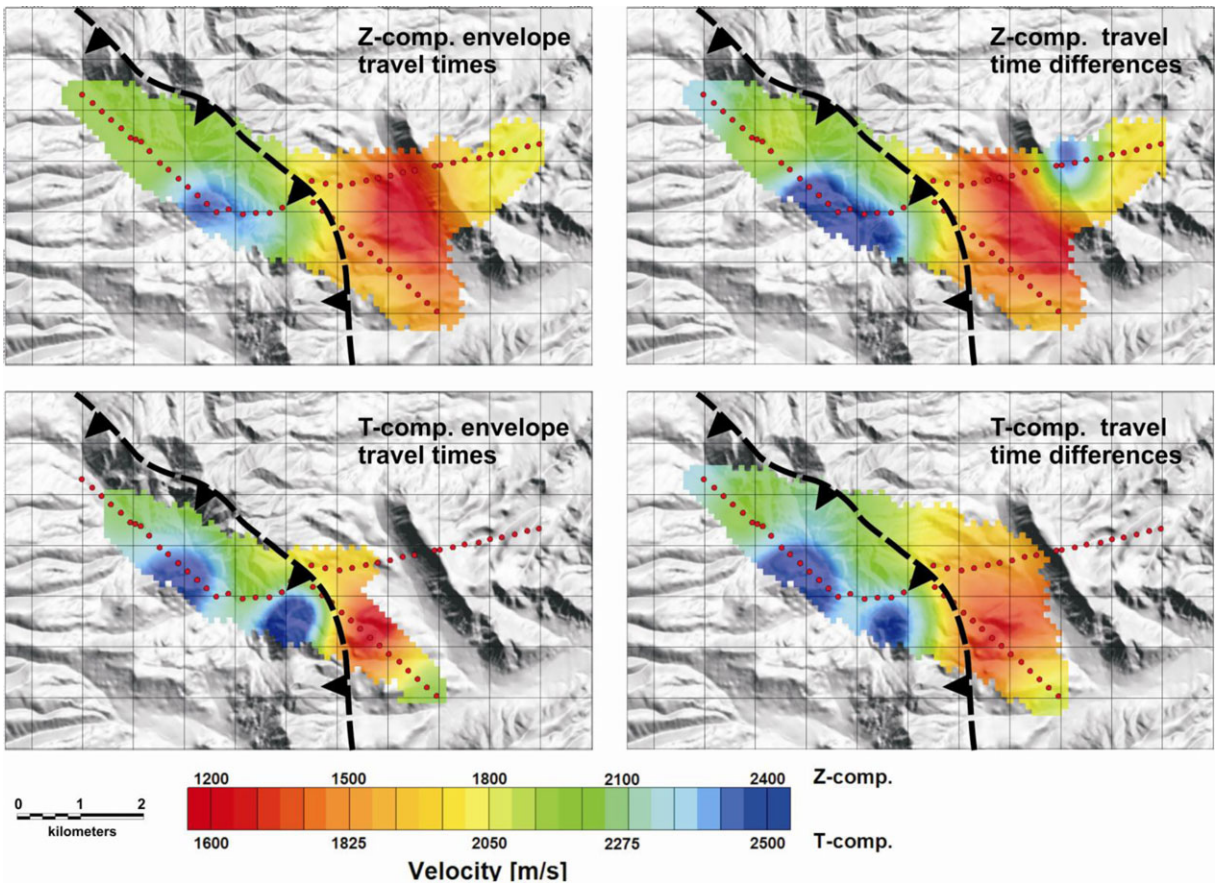

Figure 13 Results from traveltime inversion. Z- and T-component traveltimes are related to Rayleigh and Love wave velocities, respectively. Envelope traveltimes represent the Hilbert transformed interferograms and group velocities, while the traveltime differences from the original interferograms reflect phase velocities. See text for details. Note the different colour scaling for Z- and T-components. Varying coverage results from picking different virtual source – receiver combinations.

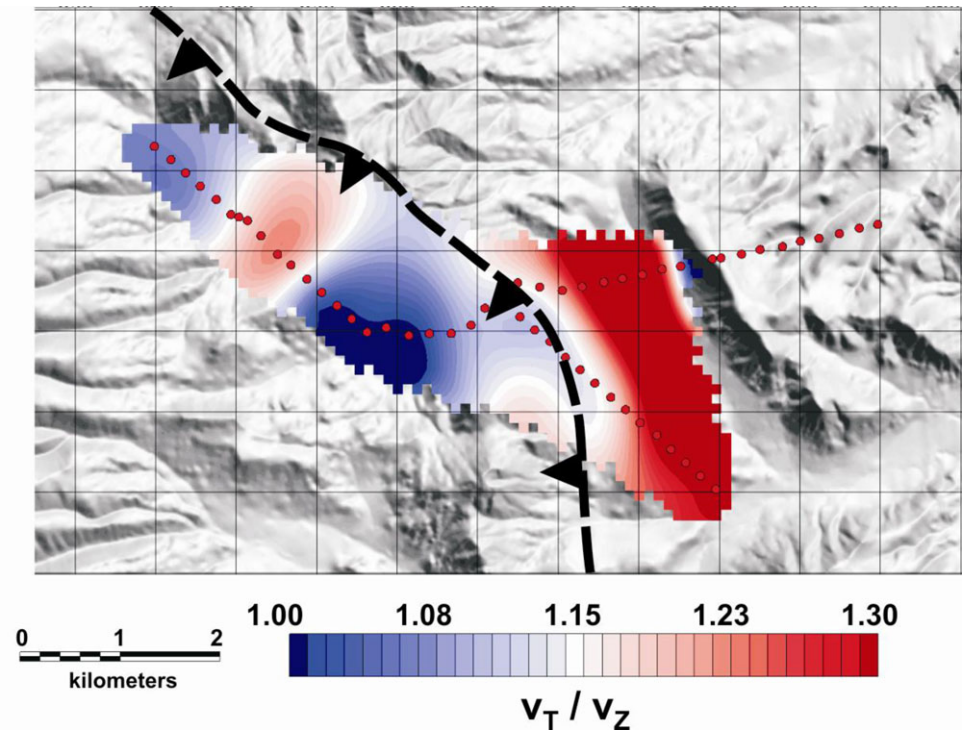

Figure 14 Ratio of Love and Rayleigh wave velocities.

The lower number of T-component traveltimes reflects the uncertainty of picking the horizontal component, which we attribute to the imperfect separation of Love and Rayleigh waves. This is also the reason why we do not include the R-component data in the inversion for Rayleigh wave velocities.

Phase velocities are associated with the interferograms prior to the Hilbert transform. As outlined before, the true onset of the phases (the absolute traveltime) is difficult to determine for most occasions but the phases can be clearly correlated over adjacent traces. Thus the traveltime difference between two adjacent traces can be estimated with comparably high accuracy and equation (6) is reformulated to express traveltime differences. In this case, the initial model is of great importance due to the relative nature of the input data and we chose the result from the group velocity inversions as initial models. Due to the effective absence of dispersion as a consequence of the limited bandwidth, we do not expect a large systematic disparity between group and phase velocities. Instead, we anticipate more localized velocity information and a larger coverage by the additional use of phase traveltime differences.

The RMS error of traveltime residuals does not significantly change after the inversion and in case of the Z-component it even slightly increases (Table 2). On the other hand, this error is considerably smaller than the RMS error of the absolute traveltimes (Table 1) and the results change only locally (Fig. 13). This implies that the limited bandwidth of the data effectively results in identical group and phase velocities. The additional use of phase traveltime differences provides improved coverage and confirms the large-scale structure of the group velocity model but some local changes to the velocity model may be regarded as possible inversion artefacts. Overall, all four inversions correlate with surface geology. The carbonates west of the Hogsback thrust are represented by higher velocities than the clay and silt stones in the east.

We estimate the depth sensitivity by the vertical eigenfunction of the surface waves (e.g., section 2.7 of Stein and Wysession 2003). The amplitude A of a Love wave as a function of depth z is proportional to:

$$A \sim \mathrm{e}^{-k_x r z}, \tag{7}$$

where k_x is the horizontal wavenumber and r is given by:

$$r = \sqrt{1 - \frac{c^2}{\beta^2}}. \tag{8}$$

c is the phase velocity of the surface wave and β is the shear-wave velocity of the bottom layer. Based on our results and previous investigation of the area, we assume a frequency of 2.5 Hz, an average Love wave velocity (c) of 2100 m/s and a

bottom layer shear-wave velocity (β) of 3000 m/s and evaluate equation (7). *A(z)* decays to a third of its maximum value at a depth of 206 m, which is approximately a quarter of the wavelength and we use this value as a rough estimate of the depth sensitivity of the surface waves. This estimation is in agreement with the layer depth calculation based on Rayleigh and Love wave velocities (e.g., section 8 of Shearer 1999). Both estimations depend on several assumptions, in particular on the poorly known bottom layer shear-wave velocities but we conclude that the observed surface waves represent average velocities from the upper 100–300 m.

We finally calculate the ratio of the Love and Rayleigh wave velocities. Due to the overall indifference of group and phase velocities, we chose the latter one because of their larger coverage (Fig. 14). The average ratio is 1.18 and the variations correlate again with surface geology with the region east of the thrust having higher values.

5 CONCLUSIONS

We successfully applied interferometry to passive seismology data from a local deployment in an industrial setting. Well-established methods from the global seismology community were adapted to the needs for local studies. Traffic noise from a state highway was the main source of the extracted surface waves. The orientation of the road with respect to the deployment results in a high number of stationary points, thus enabling a large coverage. Stacking of five days of data is sufficient to retrieve surface waves up to 5 kms of distance. Longer observation periods do not necessarily lead to better results. The S/N ratio of the interferograms is proportional to the length of the windows that are used to calculate the correlations and we find a length of 120 s sufficient for our purposes. The performance of different interferometry algorithms depends on the preprocessing. Cross-coherence is regarded as the most flexible method with respect to input data and provides robust results in this study. Both the vertical and horizontal components are of similar quality and can be used to discriminate between Love and Rayleigh waves. The limited band width prevents the calculation of depth-dependent shear-wave velocities but the high number of usable interferograms allows for inversion for laterally varying Love and Rayleigh wave velocities. These velocities correlate well with surface geology and represent the few upper hundred metres of the subsurface.

An important lesson is the relatively low amount of needed input data in areas with traffic noise. If and how the depth-sensitivity of locally excited surface waves can be increased poses an important research question. From a practical point of view, the spectral character of the noise source ultimately determines the ability to obtain dispersion curves and therefore the depth dependent structure. Ideally, a noise source spanning a sufficiently wide frequency range (perhaps from 0.5–10 Hz) will provide sufficient frequency coverage to obtain robust geological models for more sophisticated imaging applications. In a frequency limited scenario (such as ours), the models may still be useful for the calculation of near-surface shear-wave statics from surface wave velocities and large-scale geological characterization.

ACKNOWLEDGEMENTS

ExxonMobil provided funding for this study. We thank Mike Mooney (CSM), Berk Byriol, Kyle Lewallen and Jelena Tomic (ExxonMobile) for discussion and administrative support. The IRIS data management centre was used to access waveform data. Kees Wapenaar and two anonymous reviewers helped to improve the manuscript by their detailed and thoughtful comments. Data analysis was done with the software package Seismon (Mertl and Hausmann 2009), to which interferometry processing tools have been added. Codes are available from the corresponding author.

REFERENCES

Aki K. 1957. Space and time spectra of stationary stochastic waves, with special reference to micro-tremors. *Bulletin of the Earthquake Research Institute* **35**, 415–457.

Bakulin A. and Calvert R. 2006. The virtual source method: Theory and case study. *Geophysics* **71**, SI139–SI150.

Behm M., Brückl E., Chwatal W. and Thybo H. 2007. Application of stacking and inversion techniques to three-dimensional wide-angle reflection and refraction seismic data of the Eastern Alps. *Geophysical Journal International* **170**, 275–298.

Bender C.M. and Orszag S.A. 1978. *Advanced Mathematical Methods for Scientists and Engineers*. McGraw-Hill. ISBN 0387989315.

Bensen G.D, Ritzwoller M.H, Barmin M.P., Levshin A.L, Lin F., Moschetti M.P. *et al*. 2007. Processing seismic ambient noise data to obtain reliable broad-band surface wave dispersion measurements. *Geophysical Journal International* **169**, 1239–1260.

Bleistein N. 1984. *Mathematical Methods for Wave Phenomena*. Academic Press. ISBN 0121056503.

Boore D. and Toksöz M.N. 1969. Rayleigh wave particle motion and crustal structure. *Bulletin of the seismological Society of America* **59**, 331–346.

Bussat S. and Kugler S. 2009. Feasibility of Offshore Ambient-Noise Surface-Wave Tomography on a Reservoir Scale. 79th International SEG Meeting, Houston, USA, Expanded Abstracts, 1627–1631.

Denes V., Starr E.W. and Kapoor J. 2009. Developing Earth models with full waveform inversion. *The Leading Edge* **28**, 432–435.

Dong S., He R. and Schuster G.T. 2006. Interferometric Prediction and Least Squares Subtraction of Surface Waves. 76th International SEG Meeting, New Orleans, USA, Expanded Abstracts, 2783–2786.

Draganov D., Campman X., Thorbecke J., Verdel A. and Wapenaar K. 2009. Reflection images from ambient seismic noise. *Geophysics* **74**, 63–67.

Dziewonski A.M., Bloch S. and Landisman M. 1969. A technique for the analysis of transient seismic signals. *Bulletin of the seismological Society of America* **59**, 427–444.

Forghani F. and Snieder R. 2010. Underestimation of body waves and feasibility of surface-wave reconstruction by seismic interferometry. *The Leading Edge* **29**, 790–794.

Halliday D.F. and Curtis A. 2008. Seismic interferometry, surface waves and source distribution. *Geophysical Journal International* **175**, 1067–1087.

Halliday D.F., Curtis A., Robertsson J.O.A. and van Manen D.-J. 2007. Interferometric surface-wave isolation and removal. *Geophysics* **72**, A69–A73.

Iwasaki T. 2002. Extended time-term method for identifying lateral structural variations from seismic refraction data. *Earth Planets Space* **54**, 663–677.

Lak M.A., Degrande G. and Lombaert G. 2011. The effect of road unevenness on the dynamic vehicle response and ground-borne vibrations due to road traffic. *Soil Dynamics and Earthquake Engineering* **31**, 1357–1377.

Levshin A.L., Yanovskaya T.B., Lander A.V., Bukchin B.G., Barmin M.P., Ratnikova L.I. and Its E.N. 1989. *Seismic Surface Waves in a Laterally Inhomogeneous Earth. Modern Approaches in Geophysiscs, Ed. Keilis-Borok V.I.* Kluwer. ISBN 0-7923-0044-0.

Lin F., Moschetti M.P. and Ritzwoller M.H. 2008. Surface wave tomography of the western United States from ambient seismic noise: Rayleigh and Love wave phase velocity maps. *Geophysical Journal International* **169**, 1239–1260.

Mertl S. and Hausmann H. 2009. Seismon – A flexible seismic processing software. European Geosciences Union General Assembly 2009, Vienna, Austria. Geophysical Research Abstracts, EGU2009–4266.

O'Connell D.R.H. 2007. Concrete dams as seismic imaging sources. *Geophysical Research Letters* **34**, 4–8.

Paul A., Campillo M., Margerin L., Larose E. and Derode A. 2005. Empirical synthesis of time-asymmetrical Green functions from the correlation of coda waves. *Journal of Geophysical Research* **110**, B08302.

Picozzi M., Parolai S., Bindi D. and Strollo A. 2009. Characterization of shallow geology by high-frequency seismic noise tomography. *Geophysical Journal International* **176**, 164–174.

Poletto F. and Miranda F. 2004. *Seismic while drilling: Fundamentals to drill-bit seismic for exploration. Handbook of Geophysical Exploration 35*. Pergamon Press. ISBN 0-080-43928-4.

Prieto G., Lawrence J.F and Beroza G.C. 2009. Anelastic Earth Structure from the Coherency of the Ambient Seismic Field. *Journal of Geophysical Research* **114**, B07303.

Rial J.A 1989. Seismic wave resonances in 3-D sedimentary basins. *Geophysical Journal International* **99**, 81–90.

de Ridder S. and Dellinger J. 2011. Ambient seismic noise eikonal tomography for near-surface imaging at Valhall. *The Leading Edge* **30**, 1–7.

Saltzer R., Leahy G.M., Schmedes J., Roth J. and Rumpfhuber E. 2011. Earthquakes – A naturally occurring source of low frequency data. 81st International SEG Meeting, San Antonio, USA, Expanded Abstracts, 3689–3693.

Seats K., Lawrence J.F. and Prieto G.A. 2012. Improved ambient noise cross correlation functions using Welch's method. *Geophysical Journal International* **188**, 513–523.

Shearer P.M. 1999. *Introduction to Seismology*. Cambridge University Press. ISBN 0-521-66953-7.

Sirgue L. and Pratt R.G. 2004. Efficient waveform inversion and imaging: A strategy for selecting temporal frequencies. *Geophysics* **69**, 231–248.

van der Sluis A. and van der Vorst H.A. 1987. Numerical solution of large, sparse linear algebraic systems arising from tomographic problems. In: *Seismic Tomography* (eds G. Nolet and D. Reidel), pp. 49–83. Hingham. ISBN 9027725837.

Snieder R. 2004. Extracting the Green's function from the correlation of coda waves: A derivation based on stationary phase. *Physical Review E* **69**, 046610.

Snieder R. 2007. Extracting the Green's function of attenuating heterogeneous acoustic media from uncorrelated waves. *Journal of the Acoustical Society of America* **121**, 2637–2643.

Snieder R. and Safak E. 2006. Extracting the Building Response Using Seismic Interferometry: Theory and Application to the Millikan Library in Pasadena, California. *Bulletin of the Seismological Society of America* **96**, 586–598.

Snieder R., Wapenaar K. and Larner K. 2006. Spurious multiples in seismic interferometry of primaries. *Geophysics* **71**, SI111–SI124.

Song L.-P., Koch M., Koch K. and Schlittenhardt J. 2004. 2-D anisotropic Pn-velocity tomography underneath Germany using regional traveltimes. *Geophysical Journal International* **157**, 645–663.

Stehly L., Campillo M. and Shapiro N.M. 2006. A study of the seismic noise from its long-range correlation properties. *Journal of Geophysical Research* **111**, B10306.

Stein S. and Wyssesion M. 2003. *An Introduction to Seismology, Earthquakes, and Earth Structure*. Blackwell publishing. ISBN 0-86542-078-5.

Tsai V. 2011. Understanding the amplitudes of noise correlation measurements. *Journal of Geophysical Research* **116**, B09311.

Vasconcelos I. and Snieder R. 2008. Interferometry by deconvolution, Part 1: Theory for acoustic waves and numerical examples. *Geophysics* **73**, S115–S128.

Wapenaar K., Draganov D., Snieder R., Campman X. and Verdel A. 2010a. Tutorial on seismic interferometry: Part 1 – Basic principles and applications. *Geophysics* **75**, 75A195–75A209.

Wapenaar K. and Fokkema J. 2006. Green's function representations for seismic interferometry. *Geophysics* **71**, SI33–SI46.

Wapenaar K., Slob E., Snieder R. and Curtis A. 2010b. Tutorial on seismic interferometry: Part 2 – Underlying theory and advances. *Geophysics* **75**, 75A211–75A227.

Webb S.C. 1998. Broadband seismology and noise under the ocean. *Reviews of Geophysics* **36**, 105–142.